Dalton Transactions

Use of vibrational spectroscopy to identify the formation of neptunyl-neptunyl interactions: A paired Density Functional Theory and Raman spectroscopy study.

Journal:	*Dalton Transactions*
Manuscript ID	DT-ART-01-2022-000200.R2
Article Type:	Paper
Date Submitted by the Author:	26-Feb-2022
Complete List of Authors:	Pyrch, Mikaela; University of Iowa, Department of Chemistry; Augustine, Logan; University of Iowa, Chemistry Williams, James; University of Iowa, Department of Chemistry Mason, Sara; University of Iowa, Chemistry Forbes, Tori; University of Iowa, Department of Chemistry

For submission to Dalton Transactions

Use of vibrational spectroscopy to identify the formation of neptunyl-neptunyl interactions: A paired Density Functional Theory and Raman spectroscopy study.

Mikaela M. Pyrch[#] and Logan J. Augustine[#], James M. Williams, Sara E. Mason, and Tori Z. Forbes*

Department of Chemistry, University of Iowa, Iowa City, IA 52242, United States

[#]Authors contributed equally to this publication

*corresponding author: tori-forbes@uiowa.edu; 319-384-1320

Abstract: Actinyl-Actinyl interactions (AAIs) occur in pentavalent actinide systems, particularly for Np(V), and lead to complex vibrational signals that are challenging to analyze and interpret. Previous studies have focused on neptunyl-neptunyl dimeric species, but trimers and tetramers have been identified as the primary motif for extended topologies observed in solid-state materials. Our hypothesis is that trimeric and tetrameric AAIs lead to the additional signals in the vibrational spectra, but this has yet to be explored systematically. Herein, we investigate three different neptunyl-neptunyl subunits (dimeric, trimeric, tetrameric) and determine the vibrational frequencies of the O=Np=O stretches using both computational and experimental approaches. Density Functional Theory (DFT) was used to identify distinct vibrational motions related to specific neptunyl oligomers and compared to previous literature precedent from Np(V) in $HClO_4$ and HCl systems. The vibrational behavior of Np(V) in HNO_3 was then evaluated via Raman spectroscopy. As the solution evaporated signals were linked to trimeric and tetrameric models. Solid phases produced in the evaporation include $(NpO_2)_2(NO_3)_2(H_2O)_5$ and newly identified crystalline phase, $Na(NpO_2)(NO_3)_2 \bullet 4\ H_2O$ (**NpNa**). The combined computational studies and vibrational analysis provide evidence for unique observable vibrational bands for each polymerized subunit, allowing us to assign spectral features to trimeric and tetrameric models within three different simple anionic systems.

Introduction

Exploring the chemistry of the actinide elements is important for extending our knowledge of the periodic table and understanding the complexities of *f*-orbitals. This is especially relevant for the early actinides because these elements display a wide range of oxidation states and possess extended 5*f* orbitals that can contribute to bonding interactions.[1] One notable example of actinide 5*f* metal-ligand bonding occurs in the actinyl moiety (AnO_2^{n+}) where strong covalent bonding ($An{=}O_{yl}$) is observed between the actinide metal cation and oxo groups.[2] This linear *trans*-dioxo cation is the most common configuration found for the high-valent, early actinides in the penta- or hexavalent states from uranium to americium.[3, 4] The strength of $An{=}O_{yl}$ bonds are important to understanding the chemistry of these systems and is the subject of extensive experimental and theoretical studies to understand its electronic structure.[5-12] In addition, this particular bonding motif imparts significant influence on the chemistry in aqueous and solid-state systems, resulting in overall changes in its redox properties,[13, 14] disproportionation reactions,[15] and complex vibrational and electronic spectroscopy.[13, 14, 16, 17] Therefore, it is crucial to understand both the bonding within the actinyl cation and the additional interactions within the solid and solution phases to develop an in-depth, systems-level approach to the chemistry of the high-valent early actinides.

Vibrational spectroscopy is a non-destructive experimental technique that is well suited to explore actinyl bonds and interactions in these systems, but is hampered by difficulties in interpreting the complex spectra.[18, 19] For the ideal actinyl moiety with $D_{\infty h}$ symmetry, the complex typically shows one intense vibrational mode in both Raman (symmetric (ν_1) stretch) and infrared (asymmetric (ν_3) stretch) spectroscopy.[20] There also exists an infrared-active doubly-degenerate bending mode (ν_2), but this features is typically weak and found below the range of most laboratory

equipment (< 300 cm^{-1}).[21, 22] Changes in the stretching modes, through either peak shifts or activation of bands, can provide insights into bond strength of the actinide cation and the influence of intermolecular interactions. Increased σ donation to the metal center along the equatorial plane causes significant red-shifting of the ν_1 and ν_3 modes observed within the Raman and infrared spectroscopy, respectively,[23] whereas a decrease in the point-group symmetry of the system is expected to cause activation of all three vibrational modes. The symmetry of the system can be perturbed through intermolecular interactions involving the oxo groups, such as actinyl-cation (ACI), actinyl-hydrogen (AHI) and actinyl-actinyl (AAI) interactions, and lead to significant complexity within the vibrational spectra.[14, 16, 24-28]

Of particular note is AAI interactions (also known as cation-cation interactions or CCIs) because there is a significant amount of spectral complexity observed within the window of interest (600-900 cm^{-1}).[29, 30] Within systems containing $Np(V)O_2^+$, the increased Lewis basicity of the oxo groups results in a greater propensity of the neptunyl(V) unit to engage in AAIs. First discovered by Sullivan *et al.*,[13] these motifs occur when the oxo group on one neptunyl cation bonds to the neighboring neptunyl cation along the equatorial plane to form a dimeric unit (**Fig.1**). Guillaume *et al.* explored the presence of these AAIs in 1 M $HClO_4$ using Raman spectroscopy and observed the presence of an additional spectral feature that they attributed to the dimeric neptunyl-neptunyl species when Np(V) concentrates reached 0.1 M or higher.[24] With increased concentrations, they noted up to six additional vibrational modes, but did not assign them to additional neptunyl species within the solution. Since these initial studies, AAIs have been readily observed within solid-state materials and a recent review by Gilson and Burns[31] noted that 48% of the reported Np(V) compounds were built on this bonding motif. Evaluation of AAI topologies for the Np(V) solids suggests that the extended arrays are composed of repeating motifs of dimeric, trimeric, and

tetrameric subunits (**Fig. 1**). It is likely that these subunits or even larger oligomers can exist in solutions, but currently there is limited understanding of the chemical signatures that can be used to identify these species or the exact conditions that lead to their formation.

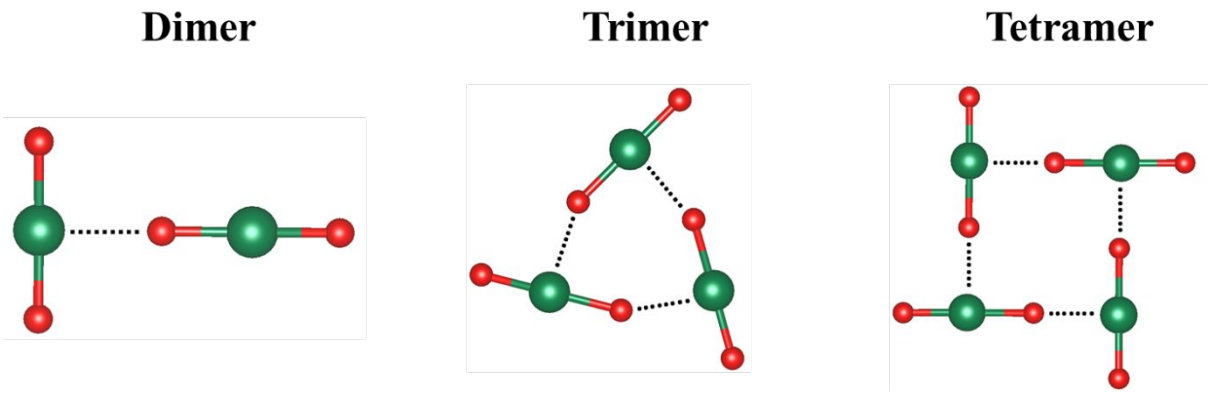

Figure 1. Ball and stick representation of the NpO_2^+ cation engaged in AAIs with the Np(V) center depicted as a green sphere and the oxygen atoms as red spheres. Polymerization of the cation is depicted in increasing order from left to right.

Given the spectral complexity is within AAI systems it is advantageous to couple experimental studies with quantum mechanical calculations to help elucidate and assign the observed vibrational modes. Previous studies have shown that Density Functional Theory (DFT) methods can accurately predict the geometric properties of the actinyl unit and its vibrational spectra.[32-37] For example, Di Pietro and Kerridge investigated the ν_1 and ν_3 modes of the uranyl unit with various equatorial ligands and found a strong correlation between the calculated red-shift of these modes with the amount of covalency occurring along the equatorial plane.[23] DFT was also used to observe the emergence of an additional ν_1 band in a Np(VI)/Li^+ system due to the occurrence of actinyl-cation interactions in solution.[16] These studies highlight the value of DFT to interpret the complex vibrational bands that arise in actinyl systems and can be applied to further understand AAIs within these systems.

In this work, Density Functional Theory (DFT) was used to systematically predict the $Np(V)O_2^+$ vibrational frequencies associated with dimeric, trimeric, and tetrameric AAI units and then compared to the Raman spectral features of $Np(V)O_2^+$ in $HClO_4$, HCl, and HNO_3 solutions. DFT calculations were benchmarked to previous experimental data and allowed us to determine the active combinational modes that can be used as chemical signatures in identifying specific AAI units and we specifically focus on modes arising from $Np=O_{yl}$ bond stretching. Raman spectroscopy was chosen as it was originally utilized by Guillaume *et al.*[24] to evaluate the formation of dimeric AAIs in solution, while Jin used it to explore the crystallization of neptunyl chloride solid phases that contain extended arrays of AAIs.[25, 26] These previous studies provide a baseline for us to then utilize Raman spectroscopy to evaluate the formation of AAIs in the $Np(V)/HNO_3$ system through a fast-evaporation process. Final products within the nitric acid system were characterized by X-ray diffraction techniques, which provides a complete picture of the formation of AAIs within solution and resulting solid phase.

Results and Discussion

Computational analysis of Np dimer, trimer, and tetrameric AAI constructs

In this work, we systematically evaluated AAIs by constructing computational models of neptunyl molecular units to determine how Np(V) vibrational features evolve through these different topological motifs. Previous theoretical studies have investigated AAIs using both DFT and wavefunction based methods.[38-44] A primary goal in each of these studies was to predict the overall stability of different AAI dimers and understand the unique bonding occurring between the two actinyl species through investigations of molecular orbitals and electron/charge transfer. Due to the unique vibrational features in IR and Raman spectroscopy that arise from these interactions in both solution and the solid-state, we use DFT to elucidate the emergence of these new

vibrational modes from additional neptunyl polymerization. Therefore, in the current study, we move beyond dimer species to also include trimer and tetramer Np(V) oligomers to expand our understanding of the bonding and vibrational modes that could be present under these conditions.

To test the suitability of the DFT exchange-correlation functional on predicting geometric and vibrational frequencies, we performed a benchmarking study of various GGA, meta-GGA, and hybrid functionals on both the monomer (Figure S1) and dimer systems (Figure 2). Full details and results from this study can be found in the Supporting Information (Figures S2-S7; Tables S1-S3). Overall, we found that GGA functionals align better to the experimental $Np{=}O_{yl}$ bond length, and ν_1 and ν_3 frequencies in the $[NpO_2(H_2O)_5]^+$ monomer system compared to meta-GGA and hybrid functionals, which both tend to underestimate the $Np{=}O_{yl}$ bond length and overestimate ν_1 and ν_3 energies in the same system. In the dimer systems, the hybrid functionals (+0.006-0.008 Å) perform better in calculating $Np{=}O_{yl}$ bond lengths (+0.006-0.008 Å) in similar systems found in solid-state structures containing neptunyl-neptunyl interactions, whereas GGA functionals overestimate this distance (+0.023-0.024 Å) (Table S1). This showed variable performance in the exchange-correlation functional in predicting $Np{=}O_{yl}$ bond lengths as a function of the number of neptunyl units in the structural models. Overall, B3LYP continued to display the best and most consistent accuracy compared to GGA functionals in larger oligomeric systems (Tables S2-S3), and is used in all the reported results.

We start with the dimeric models that are formed from the T-shaped neptunyl-neptunyl interactions (**Figure 2 top**). The Ideal model maintains the T-shape with a $Np{\cdots}O_{yl}{=}Np$ angle of 180° and the C_{2v} point group symmetry. Geometric relaxation of the Hydrated and Nitrate dimer species results in a 'bent' T-shape structure due to an internal hydrogen-bonding interaction occurring between an equatorial water ligand on one neptunyl unit and the O_{yl} on the other

neptunyl. For the Hydrated and Nitrate systems this results in the Np···O_{yl}=Np angle decreasing to 144° and 147°, respectively. Formation of the actinyl-hydrogen interaction (AHI) between the oxo group and the ligated water occurs with an O_{yl} to hydrogen distance of 1.79 and 1.75 Å in the Hydrated and Nitrate structures, respectively. This deviation from the ideal T-shape was also previously noted in computational work by McKee and Swart.[42] Formation of the AHI also changes the intermolecular Np–Np distances between the ideal and the ligated models from 4.26 Å in the Ideal T-shaped to 4.12 Å and 4.16 Å in the Hydrated and Nitrate bent T-shaped models, respectively.

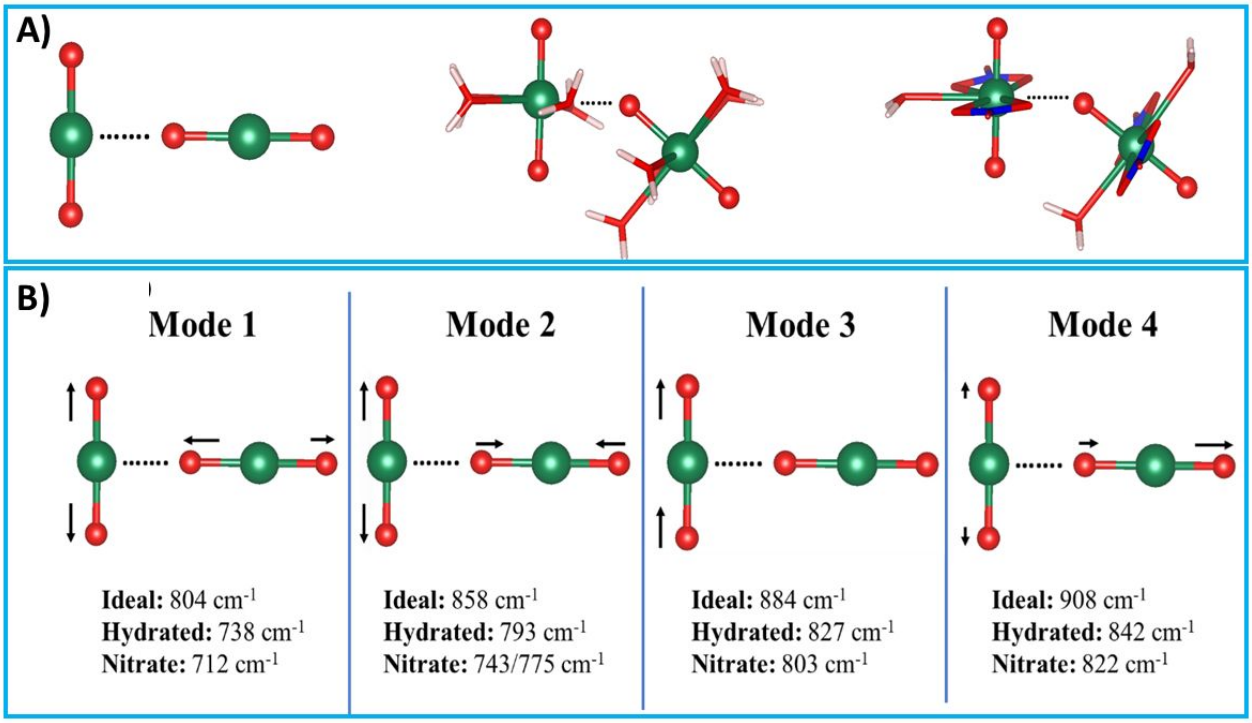

Figure 2. A) Optimized Ideal (left), Hydrated (middle), and Nitrate (right) T-shape dimer structures. Dotted lines represent the neptunyl-neptunyl interaction occurring along the equatorial plane. Atoms are represented following the same scheme as Figure 1. **B)** Calculated vibrational frequencies (with energies in cm^{-1}) for the Ideal (top), Hydrated (middle), and Nitrate (bottom) dimer species. Black vectors are used to represent the atomic motions with vector length representing the degree of motion.

Due to the formation of the dimeric species, the complexity of the vibrational modes increases as there are now additional concerted motions of the neptunyl ν_1 and ν_3 modes that need to be accounted for in the molecular unit (**Figure 2**). Of the four new neptunyl stretches that arise from this motif, the two lower energy modes involve both neptunyl units that engage in symmetric stretching (ν_1) modes, where the stretches are moving in-phase (Mode 1) and out-of-phase (Mode 2) with each other. Mode 3 is the ν_3 stretch of the neptunyl unit acting as the Lewis acid while Mode 4 in the Ideal structure is a concerted motion involving the ν_3 stretch of the neptunyl acting as the Lewis base along with a small ν_1 of the Lewis acid neptunyl. The formation of the 'bent' structure in the Hydrated and Nitrate dimers changes the atomic motions observed in the two higher energy modes (Modes 3 and 4). Both modes still display an asymmetric (ν_3) stretch on one of the neptunyl units, but this band is now coupled out-of-phase (Mode 3) and in-phase (Mode 4) with the external O_{yl} group on the other neptunyl unit. As seen with the monomer units, (see Supporting Information) the energy of the vibrational modes decreases with increased σ donation along the neptunyl equatorial plane going from Ideal to Nitrate structures.

We use the previous work by Guillaume *et al.* to compare the calculated values provided here for the Hydrated system. In their work, Np(V) is dissolved in $HClO_4$, where the neptunyl cation is not expected to coordinate to the perchlorate anion, instead forming the pentaaqua species in solution. It was observed that an increase in the Np(V) stock solution from 0.045 M to 0.1 M resulted in the appearance of a band at 738 cm^{-1} which they associated with the formation of an AAI species. This energy is identical to the value we observe for Mode 1 of the Hydrated dimer and within six wavenumbers to other reported values of the neptunyl dimer in HNO_3 (732 cm^{-1})[28] and HCl (739 cm^{-1}).[25, 26]

One additional difference for the Nitrate model is the appearance of multiple vibrational modes that arise from nitrate complexation. Mode 1 is observed at 712 cm^{-1}, which overlaps with the nitrate ν_3 modes in the same range. Mode 2 is observed at 775 cm^{-1}, but there is also a frequency at 743 cm^{-1} which has similar Np=O_{yl} stretches overlapped with a nitrate ν_4 mode. Based on the energy trends observed in the Hydrated and Ideal structures, (along with additional data in the trimer and tetramer species noted later) the frequency observed at 775 cm^{-1} is expected to be the dominant mode associated with neptunyl dimer stretching. We note there is no previous experimental vibrational spectroscopy data for the Np(V) nitrate system to compare the computation values reported herein.

From the T-shaped dimers, we build into the larger trimeric models to explore additional polymerization within the aqueous system. For the trimeric species, the three Np(V)O_2^+ units all have one oxo group involved as a Lewis base (donating) and the Np(V) behaving as the Lewis acid (accepting) to create the molecular unit (**Figure 3**). The Ideal trimer possesses C_{3h} point group symmetry and has a Np···O_{yl}=Np angle of 152°. Removal of one ligated water molecule allows for the formation of the trimeric Hydrated and Nitrate models where the Np···O_{yl}=Np changes to 150° and 151°, respectively. The Np–Np interatomic distances in the trimeric models are 4.10, 4.17, and 4.18 Å for the Ideal, Hydrated, and Nitrate systems, respectively.

Similar to the T-shape dimers, converting to the trimer species results in four unique vibrational features that involved combinations of the ν_1 and ν_3 Np=O_{yl} bond stretches (**Figure 3**). The lowest energy mode arises from each individual neptunyl unit displaying ν_1 stretches moving in-phase with each other (Mode 1). One important note for Mode 1 in this trimeric model is that the Np=O_{yl} bond stretch is not equal, as the internal O_{yl} groups that engage as the Lewis base in the unit display more atomic motion than the external O_{yl} groups. This creates a breathing-type

motion of the internal O_{yl} groups. The highest energy mode arises from each individual neptunyl unit displaying ν_3 stretches also moving in-phase with each other (Mode 4). Much like Mode 1, the degree of atomic movement varies in the Np=O_{yl} bond stretches, as now the external O_{yl} groups display more atomic motion compared to the internal groups to create a breathing mode of the external O_{yl}. Modes 2 and 3, were both doubly degenerate in energy. Mode 2 contains two neptunyl units with ν_1 stretching moving out-of-phase with each other, while the third neptunyl cation displays a ν_3 stretch. Similar to Mode 1, the internal O_{yl} groups display more atomic motion compared to the external O_{yl} groups. In Mode 3, there are two neptunyl units displaying ν_3 motions moving out-of-phase with each other, while the third neptunyl cation displays a ν_1 mode with external O_{yl} groups possessing larger atomic motions compared to internal groups as seen in Mode 4.

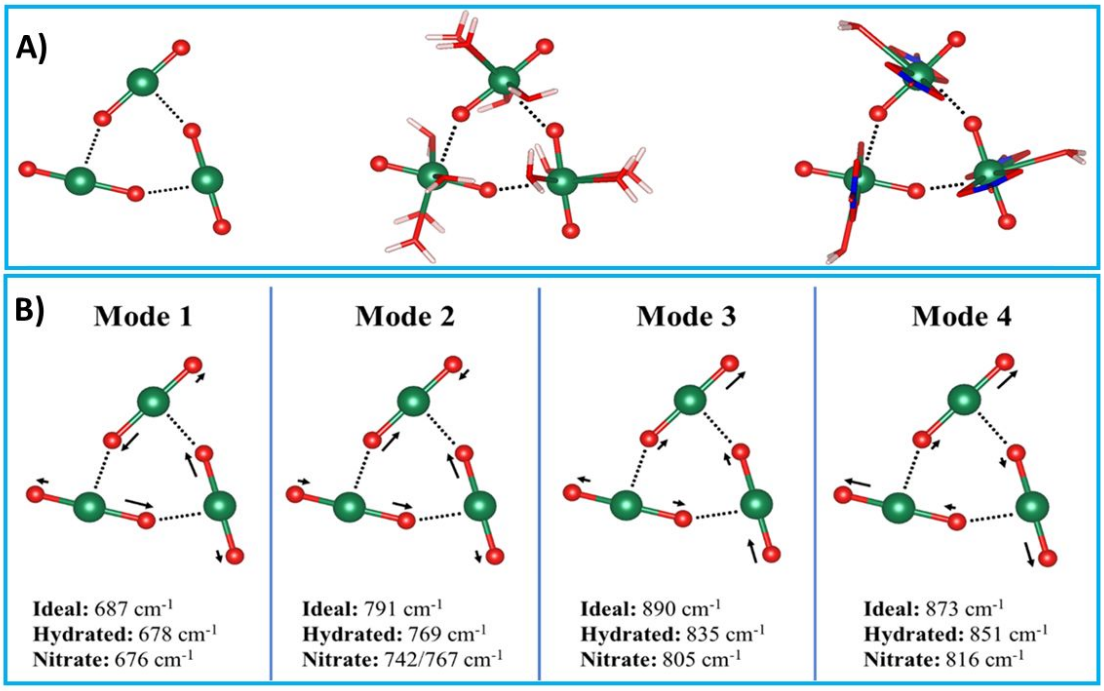

Figure 3. A) Optimized Ideal (left), Hydrated (middle), and Nitrate (right) trimer neptunyl systems. Dotted lines represent the interaction occurring along the equatorial planes. **B)** Calculated vibrational frequencies (with energies in cm^{-1}) for the Ideal (top), Hydrated (middle), and Nitrate

(bottom) trimer species. Black vectors are used to represent the atomic motions with vector length representing the degree of motion.

In the tetrameric models, each neptunyl cation in the molecular unit is also involved in a single Lewis acid and base interaction. Geometric relaxation of the Hydrated and Nitrate tetramers results in two internal hydrogen bonds forming between an equatorial H_2O ligand and an O_{yl} group on another neptunyl unit, (**Figure 3**) following what was observed in the T-shaped dimer systems. Final relaxed structures of the tetramers can be related back to the T-shaped dimers as the structures resemble the dimerization of $[(NpO_2)_2]^{2+}$, $[(NpO_2)_2(H_2O)_9]^{2+}$, and $[(NpO_2)_2(NO_3)_4(H_2O)_3]^{2-}$ systems, where the bent structure is upheld in the Hydrated and Nitrate tetramers. The Ideal system roughly maintains the C_{4h} point group symmetry with Np···O_{yl}=Np angles of 179° and Np–Np interatomic distances of 4.20 Å. The Np···O_{yl}=Np angle deviates to 149° for the Hydrated model, with additional changes of 4.14 Å for the Np–Np interatomic distances. Similar changes are observed for the Nitrate model (Np···O_{yl}=Np is 154°; 4.18 Å for Np–Np distance).

Formation of the tetramer species results in six unique vibrational modes associated with the stretching of Np=O_{yl} bonds (**Figure 4**). The lowest energy mode has each of the neptunyl units displaying ν_1 stretching in-phase (Mode 1). Similar to the trimeric models, the degree of atomic movement in this mode varies, with the O_{yl} groups engaged with the AAI exhibiting larger stretching motion compared external oxo groups, creating the internal O_{yl} breathing mode. The lowest energy mode is a combination mode of in-phase ν_1 stretching, which also follows the trend observed in both the dimer and trimer species. Similar to the other model systems, the highest energy mode of the tetramer (Mode 6) results from each individual neptunyl cation with ν_3 stretching occurring in-phase with each other. Again, the external O_{yl} groups show large atomic motion compared to those engaged in the AAI (an external O_{yl} breathing mode). Modes 3 and 4 are associated with individual neptunyl units possessing concerted ν_1 or ν_3 stretching. In Mode 3,

there are two neptunyl cations involved in ν_3 stretching in-phase with each other, but out-of-phase with the ν_3 stretching on the other two units. A similar interaction is observed in Mode 4 as two units display ν_1 modes which are in-phase with each other, but out-of-phase with the ν_1 stretching on the other monomer units. Modes 2 and 5 are doubly degenerate and display combinations of ν_1 and ν_3 stretching. The lower energy mode contains two neptunyl units with ν_1 stretching out-of-phase with each other, while the other units display ν_3 stretching which is also out-of-phase. A similar atomic motion is observed in the higher energy mode (Mode 5), but the difference between them is observed in the overall degree of motion, where Mode 2 shows large internal O_{yl} movement which transitions to large external movement in Mode 5.

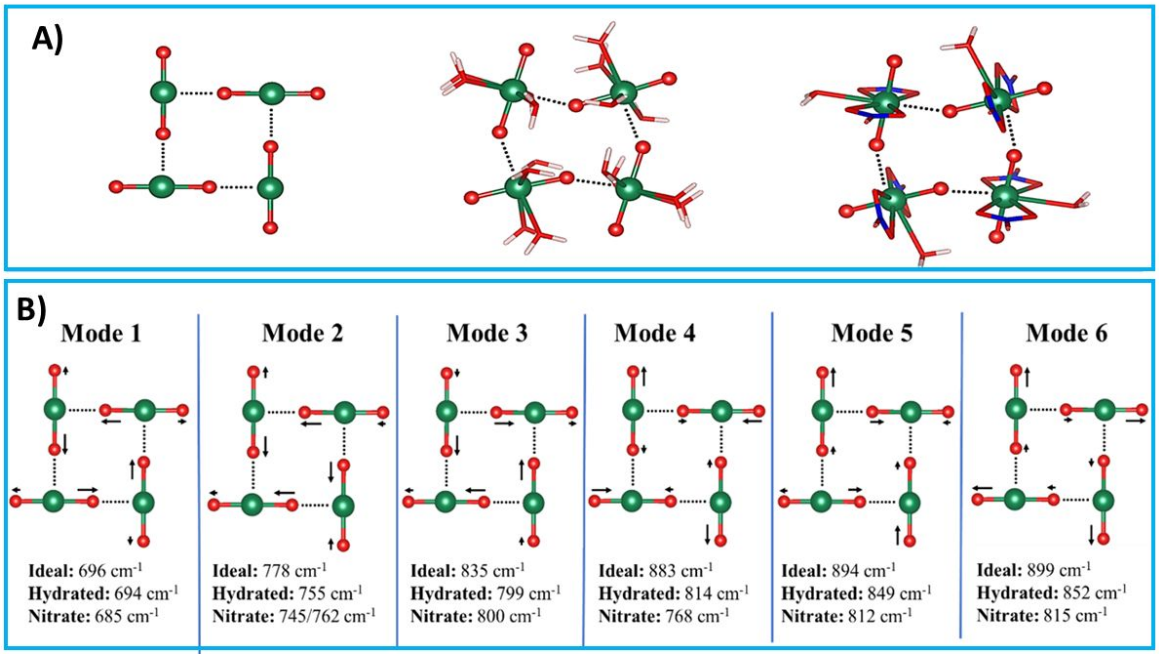

Figure 4. A) Optimized Ideal (left), Hydrated (middle), and Nitrate (right) tetramer oligomers with dotted lines, representing the neptunyl-neptunyl interaction occurring along the equatorial planes. **B)** Calculated vibrational frequencies (with energies in cm^{-1}) for the Ideal (top), Hydrated (middle), and Nitrate (bottom) tetramer species with black vectors representing the atomic motions.

There are limited experimental results in the literature to compare the modeled trimeric and tetrameric systems, but again we turn to the study by Guillaume *et al.* to evaluate the hydrated system.[24] The initial 0.045 M NpO_2^+ stock solution in 1.33 M $HClO_4$ included only the neptunyl ν_1 band at 767 cm^{-1}. As previously mentioned, increasing the Np(V) concentration to 0.18 M introduced an additional band at 738 cm^{-1} which was suggested to arise from an AAI dimer species and calculations presented herein support the formation of the T-shaped dimeric species. At higher concentrations the authors note the spectrum becomes complicated with additional overlapping features between 650-850 cm^{-1}. One peak that appears in this spectrum lies around 685 cm^{-1}, which is seen to shift towards higher energies with increasing concentrations. When compared to our predicted dimeric results, there is no evidence of a vibrational mode below 700 cm^{-1}; yet, the low energy features align well with Mode 1 of our Hydrated trimer (678 cm^{-1}) or tetrameric (694 cm^{-1}) species. At the highest Np(V) concentration, the authors note additional modes at 712 cm^{-1}, 783 cm^{-1}, and 820 cm^{-1}, but due to the peak overlap they are difficult to distinguish.

More recently, Jin performed evaporation studies of a Np(V) HCl stock solution paired with Raman spectroscopy to evaluate the solution as it crystallized to solid-state complexes with extended AAI arrays.[26] Initial solutions contained the characteristic peaks of the monomeric and dimeric species in solution, but these peaks disappeared over the course of evaporation and new features appeared with sharp intensities at 666 and 815 cm^{-1}. Upon crystallization, the lower energy peak shifted to 675 cm^{-1} with additional features forming at 800, 821, and 846 cm^{-1}. Characterization of the solid-state compounds revealed the presence of the multiple types of neptunyl-neptunyl interactions occurring within chains, sheets and framework topologies built upon tetrameric subunits. We note that the calculated Mode 1 is located within range (694 cm^{-1}) to the lowest energy feature reported by Jin and multiple bands associated with Mode 3-6 that are

were calculated between 800-850 cm^{-1}.[26] While these features do not completely align with the calculated values, this may be due to the difference in the ligand system (Cl^- versus H_2O) or the formation of larger oligiomeric clusters built from the tetramer subunit.

The work of Guillaume *et al.* and Jin demonstrated that the vibrational behavior of $Np(V)O_2^+$ becomes more complex in $HClO_4$ and HCl media, with increased vibrational signals, and correspond well to our computed modes of actinyl-actinyl-interactions.[24, 45] Within aqueous systems, our calculated vibrational modes align well with the previous Raman vibrational signals associated with the formation of a hydrated dimeric species with a bent T-shape. We also see evidence for the formation of larger oligomeric species based upon the presence of the trimeric/tetrameric Mode 1 in high concentration solutions. Due to the uniqueness of these interactions and the importance of understanding them in frequently used simple acid systems, we performed an additional experimental study to evaluate the systematic changes in the Raman vibrational spectra upon evaporation of a Np(V) nitric acid system. Characterization of the resulting products was also done to understand the formation of different oligomers in solution.

Raman Spectroscopy of the slow evaporation of NpO_2^+ in HNO_3

Slow evaporation of $Np(V)O_2^+$ in HNO_3 was performed following a similar procedure as that reported by Jin.[26] A 300uL of 85mM NpO_2^+ stock in 1.0 M HNO_3 was placed on a well-plate and then evaluated by Raman spectroscopy over the evaporation period. The background was subtracted from the collected spectra and then normalized based upon power and time. Full details are provided in the experimental section while fitted spectra are found in the supplemental information (Figure SI16-20). We divide our data into three main stages (evaporation, nucleation,

and crystallization) based upon the observed changes in solution and the resulting spectra (**Figure. 5**). Peak centroids and assignments for select spectral signals are provided in Table 1.

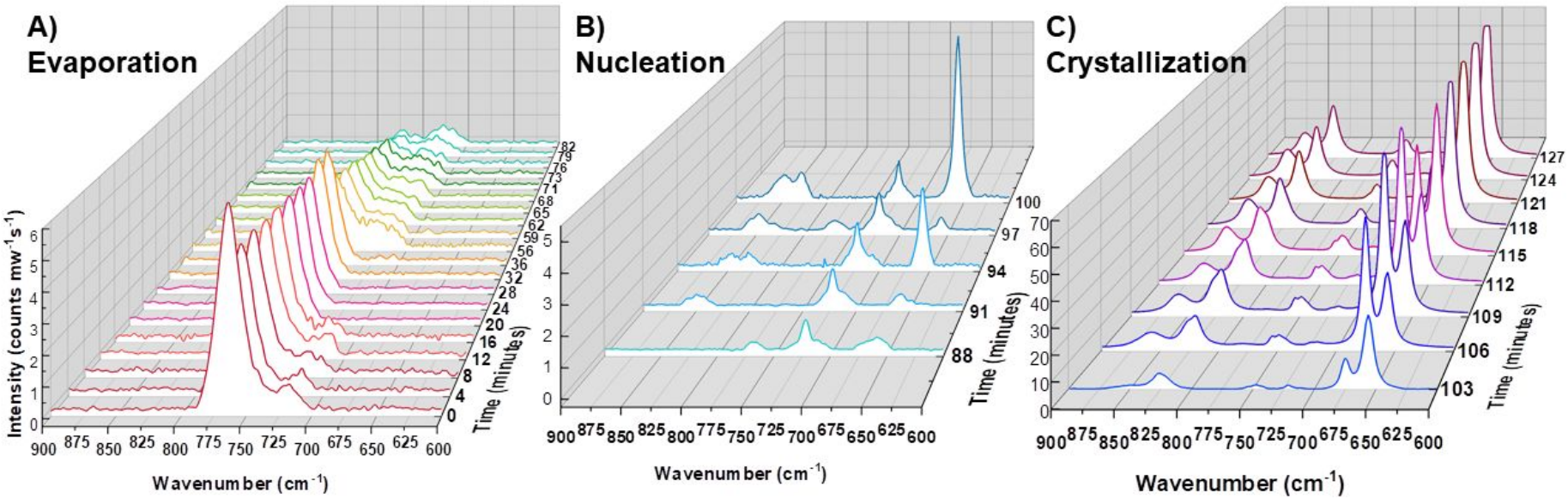

Figure 5. Normalized Raman spectra of the NpO_2^+ spectral window (600-900 cm^{-1}) in 1M HNO_3 during evaporation (A), nucleation (B), and crystallization process (C).

Table 1. Selected Raman spectral data for fast evaporation of $Np(V)O_2^+$ in HNO_3. The peak centroid (cm^{-1}) and assignments are provided for three phases (evaporation, nucleation, crystallization) of the process.

Evaporation			**Nucleation**				**Crystallization**			
0 (min)	*24 (min)*	*66 (min)*	*88 (min)*	*91 (min)*	*94 (min)*	*100 (min)*	*106 (min)*	*118 (min)*	*124 (min)*	*Assignment*
			660	658	657	655	656	656	657	Mode 1 of $[NpO_2^+]_n$
							674	675	675	Mode 1 $[NpO_2^+]_3$ nitrate
716				710	706	710	716	713	716	NO_3^- ν_3 modes
			721	722	721	723	720	720	721	NO_3^- ν_3 modes for $NaNO_3$
		738								ν_1 $[NpO_2^+]_2$ hydrate
							747	746	749	Mode 2 $[NpO_2^+]_n$ (n = 3, 4) Internal O_{yl} rocking and NO_3^- breathing
							754	754	754	Mode 2 $[NpO_2^+]_n$ (n = 3, 4) Internal O_{yl} rocking and NO_3^- breathing
767	767	767	768							ν_1 $[NpO_2(H_2O)_5]^+$
							819			Mode 4/Mode 6 (ν_3) $[NpO_2^+]_n$ (n=3, 4) nitrate
					828	827	827	825	824	Mode 6 (ν_3) of $[NpO_2^+]_n$ (n=4) hydrate/nitrate
				848	847	847				Mode 6 of $[NpO_2^+]_n$ (n=3, 4) hydrated
							857	858	857	Mode 6 of $[NpO_2^+]_n$ (n>3)

The initial spectra of the stock solution contained a band at 767 cm^{-1} that corresponds to the $[NpO_2(H_2O)_5]^+$ species and a single nitrate mode at 716 cm^{-1} (**Figure. 5a**). With evaporation of the solution, we observe an initial decrease in intensity for the neptunyl pentahydrate band and the disappearance of the nitrate feature. After 50 minutes of evaporation time (0.18 M $Np(V)O_2^+$), the $[NpO_2(H_2O)_5]^+$ signal further declines, and a broad shoulder at 738 cm^{-1} appears in the spectra. At 75 minutes of evaporation time (0.23 M $Np(V)O_2^+$), the relative intensity of these two bands changes with the signal at 738 cm^{-1} becoming more pronounced compared to the neptunyl pentahydrate band. This band at 738 cm^{-1} may be associated with a hydrated T-shape dimer as indicated by our DFT calculations and previous Raman spectroscopy. The concentration at which the dimer mode appears is similar to that reported by Guillaume *et al*. where concentrations of $Np(V)O_2^+$ greater than 0.1 M led to the appearance of the same spectral feature.[24]

After 82 minutes, the concentration of the solution is 0.26 mM NpO_2^+, and we observe a rapid change in the vibrational landscape that we associate with the nucleation process (**Figure. 5b**). During the time of nucleation, there are no observable solid phases in the solution, but changes in the vibrational spectra are evident. At the beginning of this process, the signals associated with the neptunyl pentahydrate and T-shaped dimer broaden and ultimately disappear entirely. Vibrational bands at 716 cm^{-1} and 721 cm^{-1} appear in the spectra and a broad feature simultaneously begins to take shape between 655-665 cm^{-1}. At the end of the nucleation phase, this signal resolves with a peak centroid found between 656-660 cm^{-1}. In the higher energy region of the spectral window, bands at 827 cm^{-1} and 847 cm^{-1} also appear, and their intensities continuously grow throughout evaporation of the solution.

The third region of the experiment begins when solid phases are first observed in solution, which we denote as the crystallization process. During crystallization, several new vibrational

modes appear in the spectra while the signals seen during the nucleation process become sharper and more intense. There is ingrowth of new features between 740-755 cm^{-1} that split into a dominant signal at 749 cm^{-1} with a shoulder at 754 cm^{-1}. An intense band at 675 cm^{-1} also appears during this time, but at the completion of crystallization, the strongest feature remains at 657 cm^{-1}. Within the higher energy region of the spectral window the band at 827 cm^{-1} remains relatively stable with a 3 cm^{-1} shift to 824 cm^{-1} in the final spectra, but the band at 847 cm^{-1} blue-shifts to a final position at 857 cm^{-1}. At the end of the crystallization process, the final Raman vibrational modes are positioned at 857, 824, 754, 749, 721, 716, 675 and 657 cm^{-1}.

As reference, we also performed the same experiment in the uranyl(VI) nitrate system (SI Figure S12-15). The initial spectra contains two signals at 871 and 852 cm^{-1}, that can be correlated to the uranyl pentaqua species (870 cm^{-1}) and an initial hydrolysis product $[(UO_2)_2(OH)_2]^{2+}$ (853 cm^{-1}), respectively.[46, 47] During evaporation the hydrolysis product disappears, the band at 871 cm^{-1} shifts to 868 cm^{-1} and a feature at 750 cm^{-1} appears in the spectra. Over the course of crystallization a secondary hydrolysis product reappears and the three vibrational bands remain throughout the experiments. Final band positions resolve to 867, 851, and 753 cm^{-1} and can be associated with the ν_1 for $[UO_2(H_2O)_5]^{2+}$/$[UO_2(NO_3)(H_2O)_3]^{+}$, ν_1 for $[(UO_2)_2(OH)_2]^{2+}$, and a NO_3^- ν_3 mode, respectively. (Figure S12).[47, 48]

The $Np(V)O_2^+$ system is notably more complex with eight total signals in comparison to the uranyl(VI) nitrate system with three spectral features. Hexavalent uranium will readily undergo hydrolysis when the pH is increased above 3 and can also be observed as kinetic product within solutions. Uranyl nitrate complexes are relatively weak and lower concentrations of nitrate will support the presence of hydrolysis products in the product. Neptunyl chemistry will not readily undergo hydrolysis and instead forms AAIs upon increased Np(V) concentrations. This clear

divergence of neptunyl vibrational behavior exemplifies the need for computational support in interpreting and understanding the chemistry associated with Np(V) systems.

Turning back to the DFT calculations to evaluate and assign the Raman spectra through the nucleation and crystallization process, we split our focus into the low energy (600–700 cm^{-1}), mid-energy (700–800 cm^{-1}), and high energy (800–900 cm^{-1}) regions. The dominant feature in the spectra that begins during the nucleation process and persists throughout crystallization is the band at 657 cm^{-1}. This peak is ~20-30 cm^{-1} red-shifted from the predicted lowest energy band (Mode 1) for either the trimeric (676–678 cm^{-1}) or tetrameric (685–694 cm^{-1}) species. We believe the band can be assigned to a symmetric breathing mode associated with AAI interactions. Two possible hypotheses may explain the discrepancy in the peak position between the predicted and observed spectra feature. First, it is possible that we are observing a spectral feature associated with a larger oligomer than what was modeled. Alternatively, we have observed that the best agreement between the predicted and observed vibrational energies for the monomeric and dimeric species occurs when the modeled bond distances/angles match the experimental values from the DFT benchmarking process. Therefore, it is possible that the current models are not capturing the exact sterics of the oligomers present in the nucleation and crystallization phases. During crystallization, there was an additional band in the low energy region that occurs at 675 cm^{-1}. Examining the predicted values, we see that Mode 1 for the hydrated (678 cm^{-1}) or nitrate (676 cm^{-1}) forms of the trimer agree well with this mode. Therefore, we assign this second peak in the low energy region as Mode 1 of the trimeric species (an internal O_{yl} breathing mode), although we cannot clearly differentiate between a hydrated or nitrate type species.

In the mid-energy region, there are multiple weaker bands that arise during the nucleation and crystallization process that can also be assigned to specific spectral features predicted by DFT.

The modes at 716 and 721 cm^{-1} can be assigned to the nitrate ν_3 band. The appearance of two distinct features for this mode is likely due to the presence of both a neptunyl nitrate complex and a sodium nitrate species. During the crystallization process, bands at 749 and 754 cm^{-1} also appear, and we can relate them directly to the calculated Mode 2 of either the trimeric or tetrameric species (predicted 742–767 cm^{-1}). Mode 2 for both species is a combination of internal O_{yl} rocking motion and coordinated nitrates and has two signals associated with in-phase stretching versus out of phase stretching of the two modes.

In the high energy region, bands at 847 cm^{-1} and 858 cm^{-1} are observed during the nucleation and crystallization processes, respectively which we assign to an in-phase ν_3 stretching feature. The computational studies suggest that in-phase ν_3 stretching is the highest energy mode for all our hydrated polymeric species (dimer (mode 4), trimer (mode 4), tetramer (mode 6)) and lies between 842–852 cm^{-1}. Since the distinct signal at 738 cm^{-1} associated with the hydrated dimer is no longer observed in the spectra when these modes appear, we further conclude that this vibration is the combination ν_3 of $[NpO_2^+]_n$ (n = 3, 4) species. A signal at 828 cm^{-1} also appears during nucleation and persists until the end of the experiment (final 824 cm^{-1}). Mode 6 for the hydrated tetramer is predicted to occur at 852 cm^{-1}, while the nitrate species is predicted at 815 cm^{-1}. This large difference between the Mode 6 for the hydrate and nitrate tetramer species is interesting because there should not be significant differences in σ donation to the metal center between water and nitrate.[49-51] DFT calculations were performed on a model where each $(Np(V)O_2)^+$ cation was bound to two $(NO_3)^-$ anions, but it is possible that the species in solution may contain a mix of nitrate and ligated water molecules. Using this assumption, we tentatively assign the signal at 824-828 cm^{-1} to that of the Mode 6 of $[NpO_2(NO_3)H_2O]_n$ (n=4).

Overall, we can observe that the monomeric $[NpO_2(H_2O)_5]^+$ complex forms extended networks of AAIs over the course of evaporation in a nitric acid solution through Raman spectroscopy. The T-shaped dimeric phase was observed to form when the concentration of the Np(V) reached ~0.1 M followed by the formation of larger oligomeric species upon additional evaporation. We do observe a spectral signal which we assign to the Mode 1 of an AAI oligomer at the end of the experiment. We note the formation of multiple solid phases upon crystallization as observed by the presence of green and clear/white crystals. In the next section, we provide details on the characterization of these phases using X-ray diffraction techniques and relate to the oligomeric forms predicted to occur by Raman spectroscopy.

Characterization of the solid phase by X-ray diffraction

Initial powder X-ray diffraction (PXRD) was performed on the solid product formed after fast evaporation of the Np(V) in HNO_3. Results indicated the presence of multiple phases (**SI Figure S10**) as was expected from visualization of the powder. Several of the peaks were matched to solid $NaNO_3$, which is not unexpected due to the high concentrations of HNO_3 during the evaporation process. The presence of Na^+ has previously been observed in the solution due to the use of NaOH for neptunium reprocessing which would lead to the formation of the salt upon significant evaporation.[52] This also supports our assignment of the two bands at 716 cm^{-1} and 721 cm^{-1} to two unique nitrate modes associated with $NaNO_3$ and a neptunyl nitrate species. The other major phase that was identified within the diffractogram is $(NpO_2)_2(NO_3)_2(H_2O)_5$, which was previously characterized by Grigor'ev *et al*.[53] The system contains two crystallographically unique Np(V) cations that link through AAIs to form a 1-D chain structure (**Figure 6a**). In this compound, Np2 coordinates to two nitrate ligands within the equatorial plane, forming the $[NpO_2(NO_3)_2]^-$ species with a single oxo group engaged in an AAI with the neighboring Np1 atom. Np1 completes

its equatorial coordination by further coordinating to ligated water to form $[NpO_2(H_2O)_4]^+$ units. Both oxo groups of the neptunyl moiety engage in AAIs to complete the coordination sphere of the neighboring $[NpO_2(NO_3)_2]^-$ complex, creating a 1-D chain down the [010] axis that is two neptunyl polyhedra wide. In the crystal structure, the axial $Np{=}O_{yl}$ range from 1.828 to 1.847 Å while the equatorially coordinated ligands possess bond lengths between 2.419 and 2.639 Å. The $Np{\cdots}O_{yl}{-}Np$ coordination angle is 150.8°, deviating from a perfect T-shape structure. Comparing the calculated PXRD pattern of the $NaNO_3$ and the $(NpO_2)_2(NO_3)_2(H_2O)_5$ phases to our experimental data accounted for a majority of the features in the diffractogram (Figure S10-11), but additional features that could not be completely accounted for by these two phases alone.

To induce the formation of higher quality crystalline phases, we performed a slower evaporation of the same stock solution. This resulted in the formation of a highly crystalline material (**NpNa**) that could be evaluated using single-crystal X-ray diffraction. The **NpNa** compound contains $Np(V)O_2^+$ cations engaged in AAIs to create a two-dimensional sheet topology (**Fig. 6b**). There is one crystallographically unique neptunyl cation within the unit cell and the $Np{=}O_{yl}$ distance is 1.850(4) Å. Overall, the neptunyl moieties are six-fold coordinated about the equatorial plane with an average bond distance of 2.473 Å, creating a hexagonal bipyramidal geometry. Four of the equatorial positions are associated with nitrate anions bonded in a bidentate fashion to the neptunyl cation. The anions are located on the above and below the 2-D sheet and engage in additional interactions with water molecules located in interstitial regions. The O atoms associated with nitrate anions are positionally disordered within the lattice and modeled as split sites with 50% occupancy. The other two equatorial sites are associated with neptunyl-neptunyl interactions to neighboring units and form larger trimeric species that extend the subunit into a 2-D sheet. The trimeric groups are arranged such that they create small cavities within the sheet that

are 5.94 Å in diameter. Sodium cations and water molecules are positioned within the cavities creating the overall formula of $Na(NpO_2)(NO_3)_2 \bullet 4\ H_2O$.

NpNa contains the same sheet topology observed for $La(NpO_2)_3(NO_3)_6 \bullet nH_2O$ (**NpLa**), with the major structural differences being the placement of the Na^+ and La^{3+} cations in the interlayers.[29, 54] The $Np{=}O_{yl}$ bond length for **NpLa** was reported as 1.852(4) Å with a $Np{\cdots}O_{yl}{=}Np$ angle of 149.3(2)˚. The Np–Np interatomic distances for **NpNa** and **NpLa** are 4.096(3) and 4.119 (1) Å, respectively. The similarities in bond distances, bond angles, and interatomic distances demonstrate the parallels between the **NpLa** and **NpNa** structures. We also note that the calculated powder pattern for **NpNa** does match the subtle features in the PXRD pattern obtained from the fast-evaporation process which were not previously assigned to known compounds.

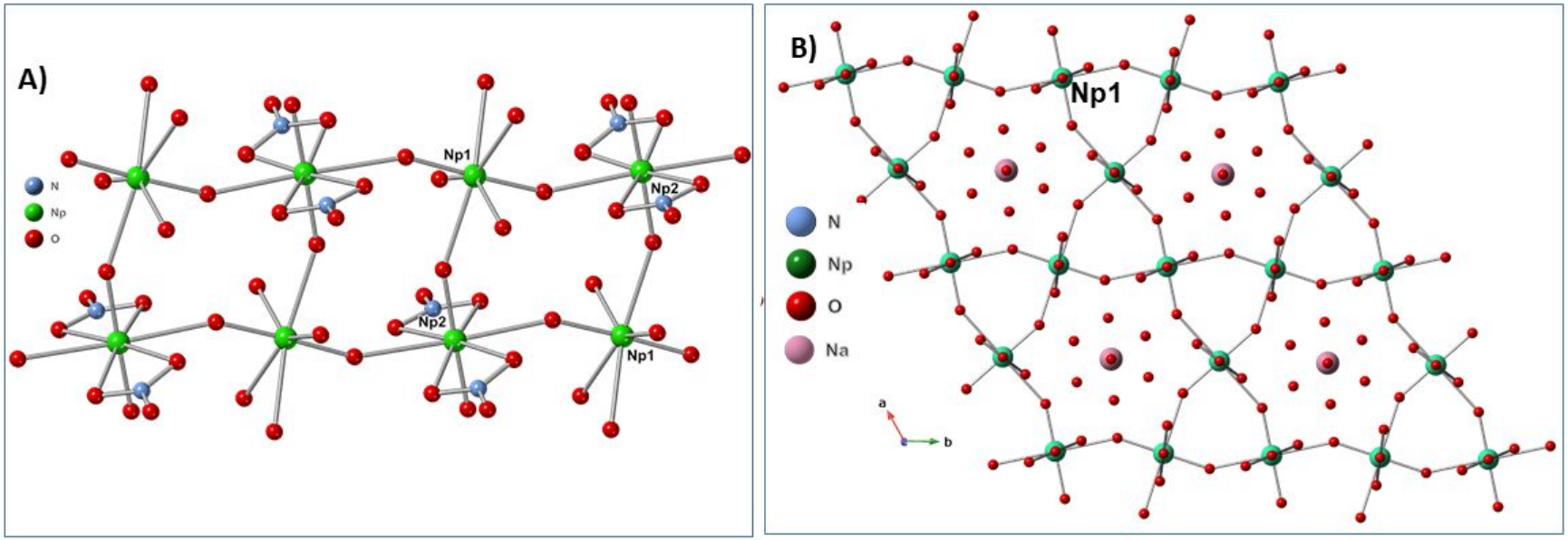

Figure 6. Ball and stick representations of the repeating motifs within $(NpO_2)_2(NO_3)_2(H_2O)_5$ (A) and **NpNa** (B) with the unique Np sites labeled. Hydrogen atoms have been removed for clarity.

Presence of $(NpO_2)_2(NO_3)_2(H_2O)_5$ and $Na(NpO_2)(NO_3)_2 \bullet 4\ H_2O$ as crystalline solids from the evaporation of $Np(V)O_2^+$ in HNO_3 corroborates the spectral interpretation that trimeric and tetrameric species formed during the nucleation and crystallization process. $(NpO_2)_2(NO_3)_2(H_2O)_5$ contains extended chains that are built upon polymerization of the tetrameric species, while $Na(NpO_2)(NO_3)_2 \bullet 4\ H_2O$ contains the trimeric group as its building unit that extends to form the 2-D sheet topology. In addition, we note that the $(NpO_2)_2(NO_3)_2(H_2O)_5$ contains $[(NpO_2)(NO_3)_2]^-$ and $[(NpO_2)(H_2O)_4]^+$ complexes within the 1-D chain. Characterization of these specific neptunyl-neptunyl interactions supports our assignment of the spectral features associated with these structures. Lastly, we see subtle differences in the bond distances for the predicted and experimental tetramer units. The axial $Np{=}O_{yl}$ range from 1.828 to 1.847 Å in the experimental structure and are observed at 1.853–1.857 Å for the calculated values. The Np–Np interatomic distances are also asymmetric within the solid-state structures (4.20 and 4.13 Å), but relatively symmetric within the optimized tetramer (Hydrated = 4.14 Å; Nitrate = 4.18 Å). These subtle differences in sterics may be the root cause of differences between the experimental and calculation values for the vibrational features, particularly for the symmetric Mode 1 band.

Lastly we note that evidence of the symmetric Mode 1 band is also observed for other Np(V) solids containing extended AAIs, with the exact position of the band related to variations in the sterics within the system.[25-27, 55, 56] $NaNpO_2(OH)_2$ was originally reported by Burns, and contains two T-shaped AAI interactions connecting together to form a corrugated 1-D chain.[25, 57] The solid-state Raman spectra of this material displayed a strong spectral feature at 635 cm^{-1} which was not specifically assigned within the study.[25, 57] In addition, $[C_{34}O_8H_{18}]_3(F,OH)_6(H_2O)_{18}(NpO_2)_{18}$ contains a 1-D Np(V) chain connected via AAIs, which combine to form a larger cluster containing

18 Np(V) centers. The resulting Raman spectrum of the solid compound contained the most intense vibration signal at 660 cm^{-1} and multiple weak features within the low-energy region of the spectral window.[58] Several other studies have reported Raman spectra with an intense low energy signal for compounds that contain extended AAI nets, including; $(NpO_2)Cl(H_2O)_2$ (675cm^{-1}), $Na_xNp^{IV}(Np^{V}O_2)_6(OH)_{1+x}\ Cl_9(H_2O)_{8-x}$ ($0 < x \leq 1$) (688 cm^{-1}), $(NpO_2)_2(C_2O_4)(H_2O)$ (654 cm^{-1}), $(NpO_2)_4Cl_4(H_2O)_6$ at (666 cm^{-1}), $Na(NpO_2)(SeO_4)(H_2O)$ at (670 cm^{-1}), $Na(NpO_2)(SO_4)(H_2O)$ at (676), $(NpO_2)_2(SO_4)(H_2O)_4$ at (676 cm^{-1}), $(NpO_2)_2(SO_4)(H_2O)_4$ (669 cm^{-1}).[25-27, 55, 56] This demonstrates that a symmetric breathing mode is likely the correct assignment, but the exact position of the peak can vary due to the specific bonding modes within the solid-state material.

Conclusions

In this work, computational and experimental methods were combined to investigate the formation of the AAIs and evaluate the impact of these interactions on the vibrational spectroscopy of the solid and solid-state materials. DFT benchmarking studies explored various exchange-correlation functionals and observed that even though GGA functionals (PBE) were better at predicting geometric and vibrational energies for the monomeric system, the use of a hybrid functional (B3LYP) was needed to properly describe these features in the larger oligomers, echoing past results reported by Katsoyannis *et al.* for Uranium systems[59] Through computational analysis, we observe the activation of multiple vibrational modes involving $Np{=}O_{yl}$ stretching beyond the typical ν_1 and ν_3 modes in the monomer system, which was a result of extended actinyl-actinyl interactions. Fast-evaporation experiments were performed to monitor the Raman frequencies associated with NpO_2^+ species in HNO_3 solutions. During the course of evaporation, we observe the formation of AAIs initially as a dimeric species in solution, but upon nucleation

and crystallization combine to form more extended trimeric and tetrameric extended networks. From the experimental results, we note the prominent peak(s) is observed in the 650-700 cm^{-1} region which was associated to Mode 1 of polymeric species.

Throughout our experiments and within the previous literature, Mode 1 is identified as concerted symmetric stretches (breathing) of $Np(V)O_2^+$ in trimeric and tetrameric coordination environments. All examples of extended neptunyl-neptunyl networks studied through Raman spectroscopy contain an intense vibrational signal in the 600-700 cm^{-1} region. This mode is sensitive to the exact coordination environment (bond lengths, angles, and sterics), and we observe it to have the most variability in the predicted peak positions. Due to this, we are interested in further exploring the sensitivity of Mode 1 for more oligomerized species and changes in AAI connectivity (e.g. diamond-shaped dimer species) in various experimental conditions. Overall, the results presented here show the value of a combined approach of theoretical calculations with experimental spectroscopy to further understand the behavior of Np(V) in simple solutions and solids. This has allowed for a more accurate understanding of the vibrational landscape and provides critical information to better interpret the Raman spectra of Np(V) solutions and solid-state compounds.

Experimental Methods

Computational Methodology

All molecular Density Functional Theory (DFT) calculations were performed using the Turbomole 7.2 software package.[60, 61] The O, N, and H atoms were represented with the polarized triple zeta (def2-TZVP) basis set[62] while Np used the def-TZVP basis set with the Stuttgart small-core (60 electrons) effective core potential (def-ECP).[63-66] To simulate the effects of an aqueous

environment, structures were embedded in an implicit solvation model, COSMO,[67] with a dielectric constant (ε) of 78.54 to represent water. To test the suitability of the DFT exchange-correlation functional on vibrational frequencies, a benchmarking study was performed on the monomer and dimer systems using various gradient corrected (GGA), meta-GGA, and hybrid functionals along with dispersion interactions. The full benchmarking results can be found in the Supporting Information (Figures S1-S7; Tables S1-S7). For each system, all atoms were allowed to fully relax without geometric or symmetry constraints during geometry optimizations and structures were converged to 5 meV/Å in the maximum norm of the gradient. Systems were embedded in COSMO during geometry optimizations; therefore, calculated gradients included forces arising from solute and screening charges. Monomer, dimer, trimer, and tetramer systems were initiated with 2, 4, 6, and 8 unpaired alpha spin orbitals, respectively, representing the high-spin state in each of these systems. A vibrational analysis for each system was conducted analytically as implemented in Turbomole and visualization of the modes was performed using TMoleX.[68] Calculated normal modes are also provided in the Supporting Information (SI Section 3).

Computational Model Systems

We began with monomer systems which were modeled as a single neptunyl cation in the absence of equatorial ligands ($[NpO_2]^+$; Ideal), bonded to five water molecules ($[NpO_2(H_2O)_5]^+$; Hydrated), or containing two nitrate anions in bidentate coordination and two water molecules ($[NpO_2(NO_3)_2(H_2O)_2]^-$; Nitrate) (**Figure S1**). For the Hydrated form, we chose five ligated water molecules based upon previous experimental and theoretical studies which suggest this is the dominant form found in solution.[49, 69-73] As the nitrate concentration in solution increases, the

ligated water molecules may be displaced by anions in the equatorial plane.[49-51] This is depicted as the Nitrate model in which the position and denticity in bonding were chosen based upon previous neptunyl nitrate coordination motifs observed experimentally and from the solid-state structure synthesized in this work.[49, 50, 54] We limited our exploration of the coordination environment around the dimeric species to two species ($[(NpO_2)(H_2O)_4]_2^{2+}$ and $[(NpO_2)(NO_3)_2(H_2O)]_2$) as previous literature for uranium from de Jong *et al.* suggested that the level of sigma donation to the metal center is similar between water and nitrate and this leads to insensitivity in the spectral features associated with coordination of nitrate to the U(VI) cation.[47, 74] While we may expect Np(V) to display subtle differences to U(VI) given the change in electronic structure, we can utilize the dimeric species we did model to understand the vibrational spectroscopy associated with the $(NpO_2)_2(NO_3)_2(H_2O)_5$ phase as $[(NpO_2)(H_2O)_4]_2^{2+}$ and $[(NpO_2)(NO_3)_2(H_2O)]_2$ are the two coordination environments observed in the $(NpO_2)_2(NO_3)_2(H_2O)_5$ phase. The Ideal systems throughout this work were generated to contain high symmetry ($D_{\infty h}$, monomer; C_{2v}, dimer; C_{3h}, trimer; C_{4h}, tetramer) and used to help with assigning vibrational modes observed in the Hydrated and Nitrate systems because inclusion of the equatorial ligands results in the overall molecular symmetry decreasing to C_1. The dimer, trimer, and tetramer oligomers were constructed from ligand exchange reactions between a neptunyl unit and equatorial water molecule, except for Ideal structures, which did not include any ligated water in the equatorial plane. With increasing Np concentrations, we would expect to observe oligomerization beyond the dimeric form, so the formation of trimers and tetramers or even larger species anticipated. Tetrameric Np AAI clusters have been previously reported by Copping *et al.* in 2012 and a similar U(V) tetramer with AAIs was reported by Burdet *et al.* in 2006.[75, 76] Final optimized coordinates of the structures can be found in the Supporting Information.

Preparation of Np(V) nitrate solution

A pure Np(V) nitrate stock solution was created by reprocessing our approximately 50 mg of ^{237}Np. ***Caution:*** *Neptunium-237 is a highly radioactive alpha emitter. All research with neptunium is restricted to specialized laboratories and must be handled under appropriate regulatory controls.* Neptunium solids were dissolved in 1M HNO_3 and then ozonolysis was performed for 12 hours to ensure that there was no Np(IV) present in the solution. This resulted in the formation of a mixed Np(V)/Np(VI) solution (based upon brownish green solution) and solid $NaNO_2$ was added reduce any Np(VI) in the experiment and create the emerald green Np(V) solution. The resulting Np(V) was precipitated with saturated NaOH, re-dissolved in 1 M $HClO_4$, and purified by a cation exchange column containing Amberchrom-50-X8 resin to remove residual metals. This purified Np(V) solution was again precipitated with minimal amounts of NaOH, rinsed three times with ultrapure H_2O, and dissolved in 1.0 M HNO_3 to serve as the Np(V) stock solution for all experiments. A Packard Tri-Carb Liquid Scintillation Counter was used to determine the concentration of the stock (85 mM) and the Np(V) oxidation state in the solution was confirmed with Raman spectroscopy (SnRI High-Resolution Sierra 2.0 Raman spectrometer).

Evaporation experiments and characterization by Raman spectroscopy

Fast evaporation studies were carried out with the Np(V) nitrate stock solution. A 100 cm watch glass was paced in a glass petri dish and placed on the main stage of the SnRI High-Resolution Sierra 2.0 Raman spectrometer equipped with 785 nm laser energy and 2048 pixels TE-cooled CCD. The $Np(V)O_2^+$ stock in 1M HNO_3 (300 μL) was added directly to the center of the watch glass and the laser was initially focused on the solution. Laser power was set to the

maximum output value of 15 mW, giving the highest achievable spectral resolution of one cm^{-1}, and the collection time was set at 60 seconds. Spectra were collected every 360 s for over three hours to monitor the change in the solution over the evaporation process. The laser was focused as needed throughout the data collection process. Upon complete evaporation of the stock solution, solid materials were observed on the bottom of the watch glass. Raman spectra at multiple positions within the watch glass were collected to confirm that the reported spectra were representative of the bulk sample. After data collection, the watch glass was carefully removed from the spectrometer and the Np(V) solid transferred to a vial for further analysis. The background was subtracted from the averaged spectral data, the counts were normalized by laser power and time, and multiple peaks were fit using the peak analysis protocol with Gaussian functions using the OriginPro 9.1.0 (OriginLab, Northampton, MA) 64-bit software. [77]

To determine the identity of the final product, the solid phase material was characterized by powder X-ray diffraction. Data was collected on a Bruker D8 Quest single crystal X-ray diffractometer using a Molybdenum source and an Oxford low temperature coldstream maintaining temperature at 100K. Crystalline materials from the fast evaporation studies were gathered on a MiTegen micromount, doubly contained, and checked for external contaminations before data were collected on the instrument. Frames were collected and Debye Rings were integrated from 2 theta of 2 to 40˚ using the Integrate Debye Rings function found within the Bruker APEX3 software.[78]

Characterization and synthesis of the solid Np(V) product

To further confirm the identity of the solid phase material obtained by powder X-ray diffraction, additional slow-evaporation experiments were performed to obtain highly crystalline

product. To form the crystalline phase, 200 μL of a 20 mM $Np(V)O_2^+$ stock solution was added to a 10 mL scintillation vial. An additional 0.002 g of solid $NaNO_3$ was added to the solution and mixed slightly to dissolve. The final solution was allowed to slowly evaporation over the course of 14 days, the resulting green-yellow crystals (**NpNa**) formed at the bottom of the vial in small yields. Due to the radioactive nature of the solid phase, it was not possible to collect quantitative yields on this phase.

Single crystals of **NpNa** were isolated and mounted on a MicroMount from MiTeGen using NVH immersion oil (Cargille Labs) for single-crystal X-ray diffraction. Structural analysis was performed on a Bruker D8 Quest single crystal X-ray diffractometer equipped with a microfocus beam (Mo Kα; λ = 0.71073 Å). Data were collected with the Bruker APEX3 software package[78] and peak intensities were corrected for (Lorentz, polarization, background effects, and absorption). The initial structure was solved by intrinsic phasing methods and refined on the basis of F^2 for all unique data using the SHELXTL version 5 series of programs.[79] Np atoms were located by direct methods and the O, N, and Na atoms were found and modeled from the difference Fourier map. The crystallographic information files for **NpNa** can be found on the Cambridge Structural Database by requesting numbers 2142993. Details on the refinement, select crystallographic parameters (Table S8), additional information on bond distances and angles (Table S9) and images depicting thermal ellipsoids and structural connectivity (Figure S8 and S9)can be found in the supporting information section.

Acknowledgments

This work was funded by the Department of Energy Basic Energy Sciences program under DE-SC0021420.

References

1. S. Ahrland, K. Bagnall and D. Brown, *The chemistry of the actinides: comprehensive inorganic chemistry*, Elsevier, 2016.
2. M. L. Neidig, D. L. Clark and R. L. Martin, *Coordination Chemistry Reviews*, 2013, **257**, 394-406.
3. G. Choppin, J.-O. Liljenzin, J. Rydberg and C. Ekberg, in *Radiochemistry and Nuclear Chemistry (Fourth Edition)*, eds. G. Choppin, J.-O. Liljenzin, J. Rydberg and C. Ekberg, Academic Press, Oxford, 2013, DOI: https://doi.org/10.1016/B978-0-12-405897-2.00014-8, pp. 405-444.
4. I. May, R. Copping, S. M. Cornet, C. E. Talbot-Eeckelears, A. J. Gaunt, G. H. John, M. P. Redmond, C. A. Sharrad, A. D. Sutton and D. Collison, *Journal of alloys and compounds*, 2007, **444**, 383-386.
5. R. G. Denning, *The Journal of Physical Chemistry A*, 2007, **111**, 4125-4143.
6. R. G. Denning, in *Complexes, Clusters and Crystal Chemistry*, Springer, Berlin, Heidelberg, 1992, vol. 79, pp. 215-276.
7. S. Matsika, Z. Zhang, S. R. Brozell, J. P. Blaudeau, Q. Wang and R. M. Pitzer, *The Journal of Physical Chemistry A*, 2001, **105**, 3825-3828.
8. O. C. Gagné, *Acta Crystallographica Section B: Structural Science, Crystal Engineering and Materials*, 2018, **74**, 49-62.
9. A. McSkimming, J. Su, T. Cheisson, M. R. Gau, P. J. Carroll, E. R. Batista, P. Yang and E. J. Schelter, *Inorganic Chemistry*, 2018, **57**, 4387-4394.
10. P. Li, H. Wei, M. Duan, J. Wu, Y. Li, W. Liu, Y. Fu, F. Xie, Y. Wu and J. Ma, *ACS omega*, 2020, **5**, 31974-31983.
11. G. Liu, S. Wang, T. E. Albrecht-Schmitt and M. P. Wilkerson, *The Journal of Physical Chemistry A*, 2012, **116**, 8297-8302.
12. M. Vasiliu, T. Jian, J. K. Gibson, K. A. Peterson and D. A. Dixon, *Inorganic chemistry*, 2020, **59**, 4554-4566.
13. J. C. Sullivan, J. C. Hindman and A. J. Zielen, *Journal of the American Chemical Society*, 1961, **83**, 3373-3378.
14. M. M. Pyrch, J. L. Bjorklund, J. M. Williams, D. L. Parr Iv, S. E. Mason, J. Leddy and T. Z. Forbes, *Dalton Transactions*, 2020, **49**, 6854-6866.
15. H. Steele and R. J. Taylor, *Inorganic Chemistry*, 2007, **46**, 6311-6318.
16. J. L. Bjorklund, M. M. Pyrch, M. C. Basile, S. E. Mason and T. Z. Forbes, *Dalton Transactions*, 2019, **48**, 8861-8871.
17. B. E. Stout, G. R. Choppin, F. Nectoux and M. Pagès, *Radiochimica Acta*, 1993, **61**, 65-68.
18. W. Runde, *photoemission*, 2000, **7**, 2.
19. J.-Y. Colle, D. Manara, T. Geisler and R. J. Konings.
20. S. McGlynn and J. Smith, *Journal of Molecular Spectroscopy*, 1961, **6**, 164-187.
21. L. J. Basile, J. C. Sullivan, J. R. Ferraro and P. LaBonville, *Appl. Spectrosc.*, 1974, **28**, 142-145.
22. G. H. John, I. May, M. J. Sarsfield, H. M. Steele, D. Collison, M. Helliwell and J. D. McKinney, *Dalton Transactions*, 2004, DOI: 10.1039/B313045B, 734-740.
23. P. Di Pietro and A. Kerridge, *Inorg Chem*, 2016, **55**, 573-583.
24. B. Guillaume, G. M. Begun and R. L. Hahn, *Inorganic Chemistry*, 1982, **21**, 1159-1166.

25. G. B. Jin, *Inorganic Chemistry*, 2013, **52**, 12317-12319.
26. G. B. Jin, *Inorganic Chemistry*, 2016, **55**, 2612-2619.
27. G. B. Jin, S. Skanthakumar and L. Soderholm, *Inorganic Chemistry*, 2012, **51**, 3220-3230.
28. A. C. Gregoire-Kappenstein, P. Moisy, G. Cote and P. Blanc, *Radiochimica Acta*, 2003, **91**, 665-672.
29. N. N. Krot and M. S. Grigoriev, *Russian Chemical Reviews*, 2004, **73**, 89-100.
30. P. C. Burns, Y. Ikeda and K. Czerwinski, *MRS bulletin*, 2010, **35**, 868-876.
31. S. E. Gilson and P. C. Burns, *Coordination Chemistry Reviews*, 2021, **445**, 213994.
32. C. Clavaguéra-Sarrio, V. Vallet, D. Maynau and C. J. Marsden, *The Journal of Chemical Physics*, 2004, **121**, 5312-5321.
33. O. Adeyiga, O. Suleiman, N. K. Dandu and S. O. Odoh, *The Journal of Chemical Physics*, 2019, **151**, 134102.
34. D. D. Schnaars and R. E. Wilson, *Inorganic Chemistry*, 2018, **57**, 3008-3016.
35. D.-C. Sergentu, T. J. Duignan and J. Autschbach, *The journal of physical chemistry letters*, 2018, **9**, 5583-5591.
36. D.-C. Sergentu, F. Gendron, E. D. Walter, S. Park, C. Capan, R. G. Surbella, C. Z. Soderquist, G. B. Hall, S. I. Sinkov and J. Autschbach, *Inorganic chemistry*, 2021.
37. M. Sundararajan, R. S. Assary, I. H. Hillier and D. J. Vaughan, *Dalton Transactions*, 2011, **40**, 11156-11163.
38. B. Vlaisavljevich, P. Miró, D. Ma, G. E. Sigmon, P. C. Burns, C. J. Cramer and L. Gagliardi, *Chemistry – A European Journal*, 2013, **19**, 2937-2941.
39. A. Łachmańska, P. Tecmer, Ö. Legeza and K. Boguslawski, *Physical Chemistry Chemical Physics*, 2019, **21**, 744-759.
40. P. Tecmer, S. W. Hong and K. Boguslawski, *Physical Chemistry Chemical Physics*, 2016, **18**, 18305-18311.
41. P. Tecmer, F. Schindler, A. Leszczyk and K. Boguslawski, *Physical Chemistry Chemical Physics*, 2020, **22**, 10845-10852.
42. M. L. McKee and M. Swart, *Inorganic Chemistry*, 2005, **44**, 6975-6982.
43. R. Feng, E. D. Glendening and K. A. Peterson, *Physical Chemistry Chemical Physics*, 2019, **21**, 7953-7964.
44. K. Newcomb, S. P. Tiwari, N. Rai and E. J. Maginn, *Physical Chemistry Chemical Physics*, 2018, **20**, 15753-15763.
45. C. Madic, G. M. Begun, D. E. Hobart and R. L. Hahn, *Inorganica Chimica Acta*, 1984, **94**, 100-102.
46. G. Lu, A. J. Haes and T. Z. Forbes, *Coordination Chemistry Reviews*, 2018, **374**, 314-344.
47. C. Nguyen-Trung, G. M. Begun and D. A. Palmer, *Inorg. Chem.*, 1992, **31**, 5280.
48. L. V. Volod'ko and L. T. Huoah, *Journal of Applied Spectroscopy*, 1968, **9**, 1100-1104.
49. A. Ikeda-Ohno, C. Hennig, A. Rossberg, H. Funke, A. C. Scheinost, G. Bernhard and T. Yaita, *Inorganic Chemistry*, 2008, **47**, 8294-8305.
50. P. Lindqvist-Reis, C. Apostolidis, O. Walter, R. Marsac, N. L. Banik, M. Y. Skripkin, J. Rothe and A. Morgenstern, *Dalton Transactions*, 2013, **42**, 15275-15279.
51. Y.-P. Yin, C.-Z. Dong and X.-B. Ding, *Chemical Physics Letters*, 2015, **635**, 134-138.
52. M. Basile, E. Cole and T. Z. Forbes, *Inorganic Chemistry*, 2018, **57**, 6016-6028.
53. M. S. Grigoriev, I. A. Charushnikova, N. N. Krot, A. I. Yanovskii and Y. T. Struchkov, *Zhurnal Neorganicheskoi Khimii*, 1994, **39**, 179.
54. M. S. Grigor'ev, I. A. Charushnikova and N. N. Krot, *Radiochemistry*, 2005, **47**, 549-551.

55. T. Z. Forbes, P. C. Burns, L. Soderholm and S. Skanthakumar, *Chemistry of Materials*, 2006, **18**, 1643-1649.
56. G. B. Jin, S. Skanthakumar and L. Soderholm, *Inorganic Chemistry*, 2011, **50**, 5203-5214.
57. P. M. Almond, S. Skanthakumar, L. Soderholm and P. C. Burns, *Chemistry of Materials*, 2007, **19**, 280-285.
58. S. E. Gilson, P. Li, J. E. S. Szymanowski, J. White, D. Ray, L. Gagliardi, O. K. Farha and P. C. Burns, *Journal of the American Chemical Society*, 2019, **141**, 11842-11846.
59. D. Reta, F. Ortu, S. Randall, D. P. Mills, N. F. Chilton, R. E. P. Winpenny, L. Natrajan, B. Edwards and N. Kaltsoyannis, *Journal of Organometallic Chemistry*, 2018, **857**, 58-74.
60. C. L. A., R. K., T. G. W. and P. J. A., *J. Chem. Phys.*, 1991, **94**, 7221.
61. S. G. Balasubramani, G. P. Chen, S. Coriani, M. Diedenhofen, M. S. Frank, Y. J. Franzke, F. Furche, R. Grotjahn, M. E. Harding, C. Hättig, A. Hellweg, B. Helmich-Paris, C. Holzer, U. Huniar, M. Kaupp, A. Marefat Khah, S. Karbalaei Khani, T. Müller, F. Mack, B. D. Nguyen, S. M. Parker, E. Perlt, D. Rappoport, K. Reiter, S. Roy, M. Rückert, G. Schmitz, M. Sierka, E. Tapavicza, D. P. Tew, C. van Wüllen, V. K. Voora, F. Weigend, A. Wodyński and J. M. Yu, *The Journal of Chemical Physics*, 2020, **152**, 184107.
62. F. Weigend, M. Häser, H. Patzelt and R. Ahlrichs, *Chemical Physics Letters*, 1998, **294**, 143-152.
63. X. Cao and M. Dolg, *Journal of Molecular Structure: THEOCHEM*, 2004, **673**, 203-209.
64. X. Cao, M. Dolg and H. Stoll, *The Journal of Chemical Physics*, 2002, **118**, 487-496.
65. M. Dolg, H. Stoll, H. Preuss and R. M. Pitzer, *The Journal of Physical Chemistry*, 1993, **97**, 5852-5859.
66. W. Küchle, M. Dolg, H. Stoll and H. Preuss, *The Journal of Chemical Physics*, 1994, **100**, 7535-7542.
67. A. Klamt and G. Schüürmann, *Journal of the Chemical Society, Perkin Transactions 2*, 1993, DOI: 10.1039/P29930000799, 799-805.
68. C. Steffen, K. Thomas, U. Huniar, A. Hellweg, O. Rubner and A. Schroer, *Journal of Computational Chemistry*, 2010, **31**, 2967-2970.
69. B. Guillaume, R. L. Hahn and A. H. Narten, *Inorganic Chemistry*, 1983, **22**, 109-111.
70. S. Skanthakumar, M. R. Antonio and L. Soderholm, *Inorganic Chemistry*, 2008, **47**, 4591-4595.
71. P. J. Hay, R. L. Martin and G. Schreckenbach, *The Journal of Physical Chemistry A*, 2000, **104**, 6259-6270.
72. J. P. Austin, M. Sundararajan, M. A. Vincent and I. H. Hillier, *Dalton Transactions*, 2009, DOI: 10.1039/B901724K, 5902-5909.
73. Z. Cao and K. Balasubramanian, *The Journal of Chemical Physics*, 2005, **123**, 114309.
74. W. A. de Jong, E. Aprà, T. L. Windus, J. A. Nichols, R. J. Harrison, K. E. Gutowski and D. A. Dixon, *The Journal of Physical Chemistry A*, 2005, **109**, 11568-11577.
75. F. Burdet, J. Pecaut and M. Mazzanti, *J. Am. Chem. Soc.*, 2006, **128**, 16512.
76. R. Copping, V. Mougel, C. Den Auwer, C. Berthon, P. Moisy and M. Mazzanti, *Dalton Transactions*, 2012, **41**, 10900-10902.
77. J. P. Picard, G. Baud, J. P. Besse and R. Chevalier, *Journal of the Less Common Metals*, 1980, **75**, 99-104.
78. G. M. Sheldrick, *Journal*, 2015.
79. G. M. Sheldrick, *Acta Crystallographica Section A: Foundations of Crystallography*, 2008, **64**, 112-122.